High-resolution photoelectron spectroscopy and photodetachment rotational simulations of SeH^- and TeH^-

Wenru Jie, Jiayi Chen, Qihan Liu, Rui Zhang, and Chuangang Ning*

Department of Physics, State Key Laboratory of Low Dimensional Quantum Physics, Frontier Science Center for Quantum Information, Tsinghua University, Beijing 100084, China

(Received 20 August 2025; accepted 8 December 2025; published 2 January 2026)

We report high-resolution slow-electron velocity-map imaging (SEVI) of cryogenically cold SeH^- and TeH^- anions. The resolved rotational structures are well reproduced by our photodetachment rotational simulations, yielding highly accurate electron affinities (EAs) of 2.212 523(27) eV for SeH, and 2.107 686(35) eV for TeH, improving the precision by a factor of more than 400 for TeH. This work demonstrates an effective approach for precisely determining electron affinities and molecular constants by combining high-resolution cryo-SEVI spectroscopy with photodetachment rotational simulations. The accurate experimental data provide benchmarks for theoretical calculations of these heavy hydrides.

DOI: 10.1103/k266-pdwr

I. INTRODUCTION

In the past decade, the development of the slow-electron velocity-map imaging method in combination with a cryogenically cold ion trap (cryo-SEVI) has greatly improved the energy resolution of the photodetachment spectroscopy of anions [1–7]. For atomic anions, peaks in the photoelectron spectra are very sharp, with widths of only a few cm^{-1}, or even less than 1 cm^{-1}, allowing the electron affinities (EAs) of atoms to be determined with an accuracy of better than 1 cm^{-1} [8–12]. However, for molecular anions, photoelectron spectra are often congested, especially for species with small rotational constants, where the rotational branches and fine-structure components overlap significantly. Peaks in a molecular photoelectron energy spectrum usually have a width of a few tens to hundreds of wave numbers, and the peak profile often deviates markedly from a Gaussian shape, causing a systematic deviation of the weighted peak center from the true EA value [13–17]. Recently, we have developed a method for photodetachment rotational simulations of molecular anions to extract their EA values with significantly improved accuracy [18].

In the present work, we apply this method to SeH^- and TeH^- anions. Diatomic hydrides typically have a large rotational constant B on the order of 10 cm^{-1}, making partial resolution of the rotational structure possible with the cryo-SEVI method. Group VIA hydrides play an important role in atmospheric chemistry, combustion, and astrochemistry. In our previous experiment on OH^-, the EA-defining transition was clearly resolved, allowing unambiguous extraction of the EA directly from the spectrum [18]. EA values and molecular constants of OH^- and SH^- have been accurately measured using high-resolution spectroscopic methods [18–21]. However, no high-resolution spectroscopic studies of the heavier congeners SeH^- and TeH^- have been reported. For SeH, in 1972, Smyth *et al.* reported its EA to be 2.21(3) eV using photoelectron energy spectroscopy [22]. Later, Stoneman *et al.* measured a series of well-separated thresholds at a high rotational quantum number J'' using threshold photodetachment of SeH^- in a Penning trap [23,24]. This approach yielded precise rotational constants, and determined the EA of SeH to be 17 845.17(20) cm^{-1} [2.212 520(25) eV] via an extrapolation method. These experimental efforts were complemented by theoretical studies, including early electron propagator calculations [25], systematic density functional theory investigations of the selenium hydrides [26], and more recent work on the spectroscopic properties and rotational constants of the SeH^- anion [27]. The only available EA(TeH) value, 2.102(15) eV, comes from the photodetachment threshold measurement by Freidhoff *et al.* [28].

In this work, we acquire high-resolution photoelectron spectra of SeH^- and TeH^- using the cryo-SEVI method at both low and room temperature. By comparing the spectra with photodetachment rotational simulations, we achieve precise determinations of their EA values and rotational constants.

II. METHODS

A. Experimental methods

The experiments were performed using our cryo-SEVI apparatus [3,6,8].SeH^- and TeH^- anions were generated by laser ablation of rotating and translating solid targets in the presence of methane gas. Specifically, SeH^- was produced by ablating a Se target using the second harmonic (532 nm) of a Nd:YAG laser while introducing CH_4 gas into the source chamber at a backing pressure of 1.6 bars. Similarly, TeH^- was generated by ablating an AsTe target under a CH_4 pressure of 2.0 bars.

*Contact author: ningcg@tsinghua.edu.cn

The generated anions were guided by a RF hexapole and trapped in a cryogenically cooled RF octupole ion trap. Helium was used as the buffer gas for collisional cooling. The temperature of the ion trap can be controlled in the range of 5–300 K. After a trapping period of 45 ms, the ions were ejected from the ion trap for photodetachment. The anions of interest were selected using a time-of-flight mass spectrometer [29], then photodetached by a pulsed tunable dye laser (repetition rate: 20 Hz; linewidth: 0.06 cm^{-1}) pumped by the second harmonic of a Nd:YAG laser. The outgoing photoelectrons were detected via a microchannel plate/phosphor screen assembly and recorded by a CCD camera. Each photoelectron image was typically an accumulated result for 50 000 laser shots. The photoelectron velocity distributions were reconstructed from the raw images using the maximum entropy velocity Legendre reconstruction (MEVELER) algorithm [30].

B. Rotational Envelope Simulations

To interpret the experimental photoelectron spectra, we performed rotational simulations of the photodetachment process. The methodology employed in this study follows that of Schulz *et al.* [31], where the rotational transition intensities are derived from quantum angular momentum coupling. A detailed derivation of this method was presented in our previous work [18]. In brief, the photodetachment process is modeled as a two-step process. In the first step, the anion absorbs a photon and is excited to a high-energy Rydberg state. In the second step, the anion undergoes detachment, resulting in a neutral molecule and a free electron.

Both SeH^- and TeH^- undergo photodetachment from a closed-shell $X\,^1\Sigma^+$ anion state to an open-shell $X\,^2\Pi$ neutral state via an *s*-wave channel. The intermediate state in this process is a $^1\Pi$ Rydberg state, as in the OH^- system [18]. The total angular momenta are denoted as J'' for the anion, J_i for the intermediate state, and J' for the neutral. The rotational transition intensity can be formally written as

$$I(J',J'') \propto \left| \sum_{J_i=J'\pm 1/2} \langle u_\alpha, J'|u_i, J_i\rangle \langle u_i^e|r|u_\beta^e\rangle \langle u_i^v|u_\beta^v\rangle \langle u_i^r, J_i|u_\beta^r, J''\rangle \right|^2, \tag{1}$$

where u_β, u_i, and u_α are the wave functions of the anion, the intermediate state, and the neutral molecule, respectively. These wave functions can be factorized into electronic (u_e), vibrational (u_v), and rotational (u_r) components. Assuming the electronic matrix element and vibrational overlap integrals (Franck-Condon factors) do not vary with the rotational quantum number, the main spectral features are dominated by rotational structures and Hönl-London factors [the last term in Eq. (1)] [32].

The energy levels of the initial $X\,^1\Sigma^+$ anion state were calculated using the standard rigid rotor formula:

$$BJ(J+1) - DJ^2(J+1)^2. \tag{2}$$

Here, B is the rotational constant, and D is the centrifugal distortion constant.

TABLE I. The matrix representation of SeH and TeH molecule Hamiltonian in the $^2\Pi$ basis.[a]

	$^2\Pi_{1/2}$	$^2\Pi_{3/2}$
$^2\Pi_{1/2}$	$-A/2 + B\left[J^2 + J - \frac{3}{4}\right]$	$B\sqrt{\left(J-\frac{1}{2}\right)\left(J+\frac{3}{2}\right)}$
$^2\Pi_{3/2}$	$B\sqrt{\left(J-\frac{1}{2}\right)\left(J+\frac{3}{2}\right)}$	$A/2 + B\left[J^2 + J - \frac{11}{4}\right]$

[a]From Eqs. (2) and (3) in Ref. [33] and the same result was also obtained from Eqs. (1-17) and (1-18) in Ref. [34].

For the $X\,^2\Pi$ neutral state, the rotational levels undergo spin-orbit coupling, and the total Hamiltonian is expressed in the Hund's case (a) basis set. The matrix representation of the Hamiltonian in the $^2\Pi$ basis is provided in Table I. Diagonalizing this Hamiltonian yields both the rotational energy levels and the eigenfunctions u_α needed to evaluate the transition intensities. The two states (mixed $^2\Pi_{1/2}$ and $^2\Pi_{3/2}$) result in rotational level structures described by [34–37]

$$\begin{aligned} {}^2\Pi_{1/2}: & B\left\{\left(J+\frac{1}{2}\right)^2 - 1 - \frac{1}{2}\left[(2J+1)^2 + Y(Y-4)\right]^{1/2}\right\} \\ & - D\left(J-\frac{1}{2}\right)^2 \cdot \left(J+\frac{1}{2}\right)^2, \\ {}^2\Pi_{3/2}: & B\left\{\left(J+\frac{1}{2}\right)^2 - 1 + \frac{1}{2}\left[(2J+1)^2 + Y(Y-4)\right]^{1/2}\right\} \\ & - D\left(J+\frac{1}{2}\right)^2 \cdot \left(J+\frac{3}{2}\right)^2. \end{aligned} \tag{3}$$

Here, Y is the ratio between the spin-orbital constant A and B: $Y{=}A/B$.

The rotational transition intensities for each channel are calculated following Eq. (11) in Ref. [31]. To correct a typographical error in the original equation, we present the revised expressions below: for $\Delta J = J' - J' = 3/2$ ($O3$ and $P1$ branches):

$$I = \frac{J''-1}{2(2J''-1)}\left(c_1\sqrt{J''} + c_2\sqrt{J''-2}\right)^2, \tag{4}$$

for $\Delta J = J' - J' = 1/2$ ($P3$ and $Q1$ branches):

$$I = \frac{J''-1}{2(2J''-1)}\left(c_1\sqrt{J''-1} - c_2\sqrt{J''+1}\right)^2 + \frac{1}{2}\left(c_1\sqrt{J''+1} + c_2\sqrt{J''-1}\right)^2, \tag{5}$$

for $\Delta J = J' - J' = -1/2$ ($Q3$ and $R1$ branches):

$$I = \frac{J''+2}{2(2J''+3)}\left(c_1\sqrt{J''+2} + c_2\sqrt{J''}\right)^2 + \frac{1}{2}\left(c_1\sqrt{J''} - c_2\sqrt{J''+2}\right)^2, \tag{6}$$

for $\Delta J = J' - J' = -3/2$ ($R3$ and $S1$ branches):

$$I = \frac{J''+2}{2(2J''+3)}\left(c_1\sqrt{J''+1} - c_2\sqrt{J''+3}\right)^2. \tag{7}$$

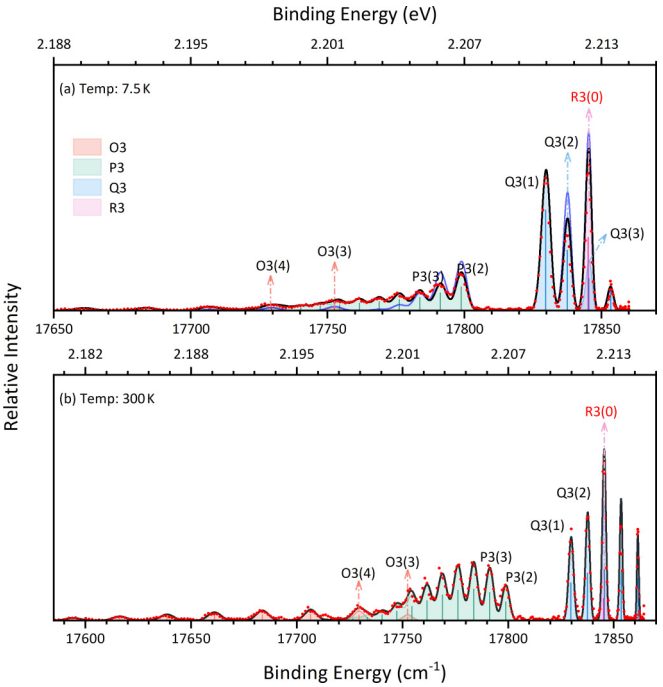

FIG. 1. Photoelectron energy spectra of SeH^-. The red dots are experimental data. (a) Spectrum obtained at temperature T= 7.5 K and a detachment laser wave number of 17 859.65 cm^{-1}. The black curve represents the simulated photoelectron spectrum with the initial rotational population shown in Fig. 3 of SeH^-, while the blue line assuming Boltzmann distribution at 80 K. The *O*/*P*/*Q*/*R* branches correspond to $\Delta N = -2/-1/0/+1$ transitions between anionic and neutral states, respectively (where N denotes the total angular quantum number without spin). The label "3" represents the $^2\Pi_{3/2}$ state of SeH. The numbers in parentheses represent the rotational quantum number N of SeH^-. The label "*R*3(0)" specifically denotes the EA photodetachment channel of SeH. (b) Comparison of experimental (red dots) and simulated (black curve) spectrum at T = 300 K and a detachment laser wave number of 17 863.69 cm^{-1}. The Boltzmann temperature used in simulation is 360 K.

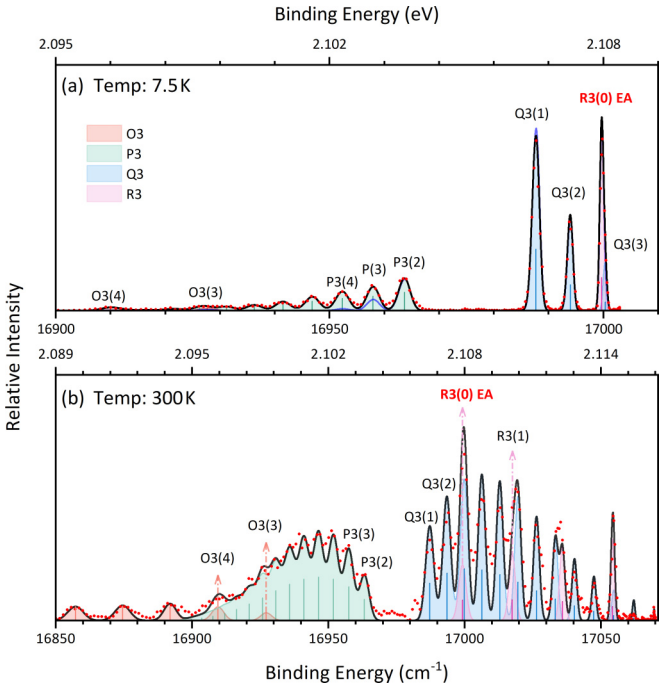

FIG. 2. Photoelectron energy spectra of TeH^-. The red dots are experimental data. (a) Spectrum obtained at temperature T= 7.5 K and a detachment laser wave number of 17 002.99 cm^{-1}. The black curve represents the simulated photoelectron spectrum with the initial rotational populations shown in Fig. 3 of TeH^-, while the blue line assuming Boltzmann distribution at 32 K. The *O*/*P*/*Q*/*R* branches correspond to $\Delta N = -2/-1/0/+1$ transitions between anionic and neutral states, respectively (where N denotes the total angular quantum number without spin). The label "3" represents the $^2\Pi_{3/2}$ state of TeH. The numbers in parentheses represent the rotational quantum number N of TeH^-. The label "*R*3(0)" specifically denotes the EA photodetachment channel of TeH. (b) Comparison of experimental (red dots) and simulated (black curve) spectrum at T = 300 K and a detachment laser wave number of 17 070.12 cm^{-1}. The Boltzmann temperature used in simulation is 380 K.

Here, c_1 and c_2 are the coefficients of SeH and TeH eigenstates expressed in the Hund's case (a) basis set,

$$c_{1a} = \left(\frac{X-2+Y}{2X}\right)^{1/2}, \quad c_{2a} = \left(\frac{X+2-Y}{2X}\right)^{1/2},$$
$$c_{1b} = \left(\frac{X+2-Y}{2X}\right)^{1/2}, \quad c_{2b} = -\left(\frac{X-2+Y}{2X}\right)^{1/2}, \tag{8}$$

the subscripts a and b denote states dominated by the $^2\Pi_{3/2}$ and $^2\Pi_{1/2}$ configurations, respectively, And

$$X = \left[4\left(J'+\frac{1}{2}\right)^2 + Y(Y-4)^{1/2}\right]^{1/2}. \tag{9}$$

III. RESULTS AND DISCUSSION

Photoelectron spectra of SeH^- and TeH^- were acquired at nominal temperatures of 7.5 and 300 K, as shown in Figs. 1 and 2, respectively. Owing to their relatively large rotational constants and simple electronic structures, both spectra exhibit partially resolved rotational transitions. At the photon energies used in this study, only the lower spin-orbit component ($^2\Pi_{3/2}$) of the neutral state is accessed due to the large spin-orbit splitting in both SeH and TeH. The $^2\Pi_{3/2}$ component exhibits negligible Λ doubling, further simplifying the spectral analysis. In the spectra, the EA photodetachment channel labeled as *R*3(0), i.e., the transition from the anionic ground state ($X\,^1\Sigma^+$, $J'=0$) to the neutral ground state ($X\,^2\Pi_{3/2}$, $J'=3/2$), overlaps with the transition $Q3(3)$ ($X\,^1\Sigma^+$, $J'=3 \rightarrow X\,^2\Pi_{3/2}$, $J'=7/2$) for both species, preventing a direct EA measurement from the peak center.

To extract EA values and rotational constants, we simulated the spectra using our approach we developed previously. The reported uncertainties (1σ) originate from multiple sources combined in quadrature, including the statistical fitting error, the laser wavelength calibration (± 0.06 cm^{-1}), the energy calibration of the spectrometer, and uncertainties

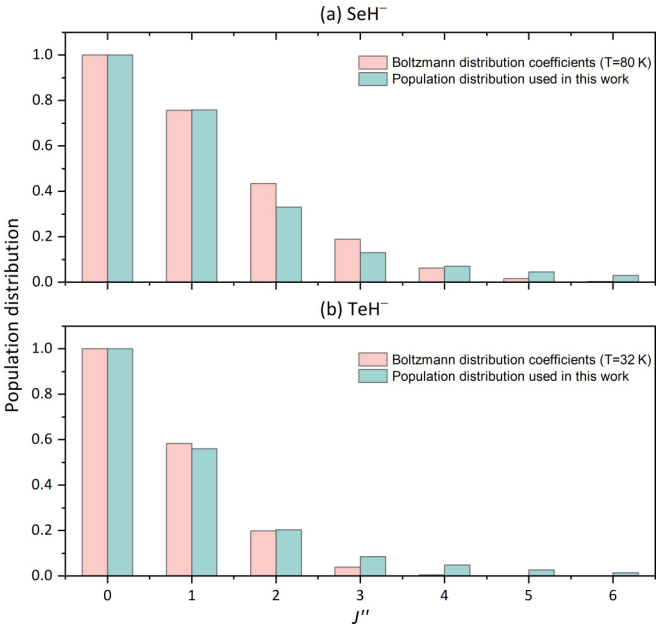

FIG. 3. Rotational populations used for the best fitting (pink) in comparison with the Boltzmann distributions (green) for (a) SeH^- and (b) TeH^-, both shown without multiplying the rotational degeneracy factors. Experimental distributions were extracted from the best-fit simulations of cryo-SEVI spectra acquired at an ion trap temperature of 7.5 K. The Boltzmann distributions are calculated using the temperature 80 and 32 K for SeH^- and TeH^-, respectively.

in the literature constants for the neutral species. The room-temperature spectra [Fig. 1(b)] were simulated assuming a Boltzmann distribution of rotational states, yielding best-fit effective temperatures of 360 K for $^{80}SeH^-$ and 380 K for $^{130}TeH^-$. The cold spectra acquired at 7.5 K [Figs. 1(a) and 2(a)] exhibit a significant deviation from Boltzmann distributions. Similar deviations have been found in cryo-SEVI studies of OH^- and are attributed to incomplete thermalization and the RF-induced micromotion [38]. To simulate the cold spectra, we manually adjusted the populations at each rotational state for the best fit. Figure 3 shows the obtained rotational distributions from this method in comparison with Boltzmann distributions. The observed distributions at high J'' are higher than the Boltzmann distributions.

The EA(SeH) is determined to be 17 845.19(22) cm^{-1} [2.212 523(27) eV], which is in excellent agreement with the value 17 845.17(20) cm^{-1} reported by Stoneman *et al.* [24]. They measured a series of well-separated O-branch thresholds at high J'' by scanning the wavelength of the photodetachment laser in a Penning trap. This method enabled precise determination of several rotational thresholds (see Table III in Ref. [24]), from which the precise rotational constants B and D were derived and subsequently used to extrapolate an EA of 17 845.17(20) cm^{-1}. The EA channel $R3(0)$ was not directly observed due to spectral congestion. We also extract rotational constants $B = 7.7305(70) cm^{-1}$ and $D = 3.1(10) \times 10^{-4}$ cm^{-1} for SeH^-. Table II lists the molecular constants of SeH used in the simulation and those obtained for SeH^-.

TABLE III. Constants used in the photodetachment rotational simulation of $^{130}TeH^-$.

Species	A	B	$10^4 \times D$
TeH[a]	−3816.38124(43)	6.065439(26)	1.8881(17)
TeH^-[b]		6.006(6)	1.99(20)

[a]From Ref. [40].
[b]This work.

For TeH^-, the photoelectron spectrum displays more intense and closely spaced Q and R branch transitions near threshold [Fig. 2(b)], which provide stronger constraints for fitting. EA(TeH) is determined to be 16 999.63(28) cm^{-1} [2.107 686(35)] eV, which is in good agreement with the previously reported EA of 2.102(15) eV by Freidhoff *et al.* [28]. Table III lists the molecular constants of TeH used in the simulations, and rotational constants $B = 6.006(6)$ cm^{-1} and $D = 1.99(20) \times 10^{-4}$ cm^{-1} for TeH^- obtained from the simulations.

Finally, we take note of the recent proposal by Blondel and Drag of a "quantum offset" in velocity imaging-based electron spectrometry, which could introduce slight shifts in measured photoelectron kinetic energies [41]. However, we believe that such an offset is not present in properly reconstructed SEVI data such as the present results, based on our recent simulations and experimental analyses (see Ref. [12]).

IV. CONCLUSIONS

In conclusion, high-resolution photoelectron energy spectra of SeH^- and TeH^- were obtained using cryo-SEVI. Combined with photodetachment rotational simulations, accurate electron affinities of SeH and TeH and rotational constants of SeH^- and TeH^- were determined. We report electron affinities (EAs) of 2.212 523(27) eV for SeH, and 2.107 686(35) eV for TeH. The derived rotational constants are $B = 7.7305(70)$

TABLE II. Constants used in the photodetachment rotational simulation of $^{80}SeH^-$. A is the spin-orbital constant (cm^{-1}), B is the rotational constant (cm^{-1}) for $v = 0$, and D is centrifugal distortion constant (cm^{-1}).

A (SeH)	B (SeH)	$10^4 \times D$ (SeH)	B (SeH^-)	$10^4 \times D$ (SeH^-)
−1763.27345 [a]	7.7892244(836) [a]	3.37581(830) [a]	7.7305(70) [b]	3.1(10) [b]
			7.7289(46) [c]	3.33(9) [c]

[a]From Table 4 in Ref. [39].
[b]This work.
[c]From Ref. [18].

cm^{-1} and $D = 3.1(10) \times 10^{-4}$ cm^{-1} for SeH^-, and $B = 6.006(6)$ cm^{-1} and $D = 1.99(20) \times 10^{-4}$ cm^{-1} for TeH^-.

The present work highlights the power of combining cryo-SEVI spectroscopy with quantum rotational simulations in resolving spectral congestion. This approach provides a general strategy for high-precision spectroscopic measurements of molecular anions. These accurate experimental data can also serve as benchmarks for *ab initio* calculations for heavy hydrides.

ACKNOWLEDGMENT

This work was supported by the National Natural Science Foundation of China (NSFC) (Grants No. 12374244 and No. 12341401).

DATA AVAILABILITY

The data that support the findings of this article are openly available [42].

[1] J. Czekner, G. V. Lopez, and L. S. Wang, High resolution photoelectron imaging of UO^- and UO_2^- and the low-lying electronic states and vibrational frequencies of UO and UO_2, J. Chem. Phys. **141**, 244302 (2014).

[2] M. L. Weichman and D. M. Neumark, Slow photoelectron velocity-map imaging of cryogenically cooled anions, Annu. Rev. Phys. Chem. **69**, 101 (2018).

[3] R. L. Tang, X. L. Chen, X. X. Fu, H. Wang, and C. G. Ning, Electron affinity of the hafnium atom, Phys. Rev. A **98**, 020501(R) (2018).

[4] R. L. Tang, X. X. Fu, and C. G. Ning, Accurate electron affinity of Ti and fine structures of its anions, J. Chem. Phys. **149**, 134304 (2018).

[5] R. L. Tang, R. Si, Z. J. Fei, X. X. Fu, Y. Z. Lu, T. Brage, H. Liu, C. Chen, and C. Ning, Candidate for laser cooling of a negative ion: High-resolution photoelectron imaging of Th^-, Phys. Rev. Lett. **123**, 203002 (2019).

[6] R. L. Tang, R. Si, Z. J. Fei, X. X. Fu, Y. Z. Lu, T. Brage, H. Liu, C. Chen, and C. Ning, Observation of electric-dipole transitions in the laser-cooling candidate Th^- and its application for cooling antiprotons, Phys. Rev. A **103**, 042817 (2021).

[7] R. Zhang, Y. Z. Lu, S. T. Yan, and C. G. Ning, Energy levels and transition rates of the laser-cooling candidate Th^-, Phys. Rev. A **111**, 023102 (2025).

[8] C. G. Ning, Electron affinities of atoms and structures of atomic negative ions, J. Phys. Chem. Ref. Data **51**, 021502 (2022).

[9] S. T. Yan, Y. Z. Lu, R. Zhang, and C. G. Ning, Electron affinities in the periodic table and an example for As, Chin. J. Chem. Phys. **37**, 1 (2024).

[10] R. L. Tang, X. X. Fu, Y. Z. Lu, and C. G. Ning, Accurate electron affinity of Ga and fine structures of its anions, J. Chem. Phys. **152**, 114303 (2020).

[11] R. Zhang, W. R. Jie, J. Y. Chen, Q. H. Liu, and C. G. Ning, Revisiting the electron affinity of selenium, arXiv:2506.10300.

[12] R. Zhang, S. T. Yan, W. R. Jie, J. Y. Chen, Q. H. Liu, and C. G. Ning, Evaluation of quantum offset in velocity imaging-based electron spectrometry, arXiv:2510.17204.

[13] R. Klingeler, N. Pontius, G. Lüttgens, P. S. Bechthold, M. Neeb, and W. Eberhardt, Photoelectron spectroscopy of GdO^-, Phys. Rev. A **65**, 032502 (2002).

[14] G. Aravind, M. Nrisimhamurty, R. G. Mane, A. K. Gupta, and E. Krishnakumar, Probing electronic states of TaC and observation of a stable excited state of TaC^- by anion-photoelectron spectroscopy, Phys. Rev. A **92**, 042503 (2015).

[15] S. T. Yan, R. Zhang, Y. Z. Lu, and C. G. Ning, Spectroscopic observation of Feshbach resonances in the tellurium dimer anion, J. Chem. Phys. **160**, 064303 (2024).

[16] S. T. Yan, R. Zhang, and C. G. Ning, Precision measurement of the electron affinity of chlorine via high-resolution photoelectron spectroscopy, J. Phys. Chem. Lett. **15**, 7735 (2024).

[17] R. Zhang, S. T. Yan, H. W. Song, H. Guo, and C. G. Ning, Probing the activated complex of the $F + NH_3$ reaction via a dipole-bound state, Nat. Commun. **15**, 3858 (2024).

[18] W. R. Jie, J. Y. Chen, R. Zhang, S. T. Yan, and C. G. Ning, Rotational envelope simulations in photodetachment spectroscopy: Precise measurement of electron affinity of NO and O_2, J. Chem. Phys. **163**, 044309 (2025).

[19] P. A. Schulz, R. D. Mead, P. L. Jones, and W. C. Lineberger, OH^- and OD^- threshold photodetachment, J. Chem. Phys. **77**, 1153 (1982).

[20] W. Chaibi, C. Delsart, C. Drag, and C. Blondel, High precision measurement of the ^{32}SH electron affinity by laser detachment microscopy, J. Mol. Spectrosc. **239**, 11 (2006).

[21] M. DeWitt, M. C. Babin, and D. M. Neumark, High-resolution photoelectron spectroscopy of vibrationally excited OH^-, J. Phys. Chem. A **125**, 7260 (2021).

[22] K. C. Smyth and J. I. Brauman, Photodetachment of an electron from selenide ion; the electron affinity and spin-orbit coupling constant for SeH, J. Chem. Phys. **56**, 5993 (1972).

[23] R. C. Stoneman and D. J. Larson, Photodetachment spectroscopy of SeH^- in a magnetic field, J. Phys. B: At. Mol. Phys. **19**, L405 (1986).

[24] R. C. Stoneman and D. J. Larson, Rotational photodetachment spectroscopy of the SeH^- ion, Phys. Rev. A **35**, 2928 (1987).

[25] J. V. Ortiz, Applications of electron propagator theory to the electron affinities of AsH_2, SeH, Br, SbH_2, TeH, and I, J. Chem. Phys. **87**, 1701 (1987).

[26] W. G. Xu, W. J. Bai, and S. X. Lu, Structures, thermochemistry and electron affinities of the selenium hydrides SeH_n/SeH_n^- ($n = 1$–5), Chem. J. Chin. Univ. **29**, 2281 (2008).

[27] M. J. Wan, F. T. Liu, and D. H. Huang, Spectroscopic and transition properties of SeH^- anion including spin-orbit coupling, Acta Phys. Sin. **70**, 033101 (2021).

[28] C. B. Freidhoff, J. T. Snodgrass, J. V. Coe, K. M. McHugh, and K. H. Bowen, Negative ion photoelectron spectroscopy of TeH^-, J. Chem. Phys. **84**, 1051 (1986).

[29] W. C. Wiley and I. H. McLaren, Time-of-flight mass spectrometer with improved resolution, Rev. Sci. Instrum. **26**, 1150 (1955).

[30] B. Dick, Inverting ion images without Abel inversion: Maximum entropy reconstruction of velocity maps, Phys. Chem. Chem. Phys. **16**, 570 (2014).

[31] P. A. Schulz, R. D. Mead, and W. C. Lineberger, Rotational intensities in photodetachment and photoionization, Phys. Rev. A **27**, 2229 (1983).

[32] A. Hansson and J. K. G. Watson, A comment on Hönl-London factors, J. Mol. Spectrosc. **233**, 169 (2005).

[33] T. E. H. Walker, P. M. Dehmer, and J. Berkowitz, Rotational band shapes in photoelectron spectroscopy: HF and DF, J. Chem. Phys. **59**, 4292 (1973).

[34] J. T. Hougen, *The Calculation of Rotational Energy Levels and Rotational Line Intensities in Diatomic Molecules* (National Bureau of Standards, Washington, DC, 1970).

[35] F. Breyer, P. Frey, and H. Hotop, High resolution photoelectron spectrometry of negative ions: Rotational transitions in laser-photodetachment of OH^-, SH^-, SD^-, Z. Phys. A **300**, 7 (1981).

[36] H. Hotop, T. A. Patterson, and W. C. Lineberger, High resolution photodetachment study of OH^- and OD^- in the threshold region 7000–6450 Å, J. Chem. Phys. **60**, 1806 (1974).

[37] T. C. James and R. J. Thibault, Spin-orbit coupling constant of nitric oxide. determination from fundamental and satellite band origins, J. Chem. Phys. **41**, 2806 (1964).

[38] R. Wild, M. Nötzold, M. Simpson, T. D. Tran, and R. Wester, Tunnelling measured in a very slow ion-molecule reaction, Nature (London) **615**, 425 (2023).

[39] R. S. Ram and P. F. Bernath, Fourier transform infrared emission spectroscopy of SeH, J. Mol. Spectrosc. **203**, 9 (2000).

[40] S. Yu, A. Shayesteh, D. Fu, and P. F. Bernath, Infrared and near infrared emission spectra of TeH and TeD, J. Mol. Spectrosc. **230**, 105 (2005).

[41] C. Blondel and C. Drag, Quantum offset of velocity imaging-based electron spectrometry and the electron affinity of arsenic, Phys. Rev. Lett. **134**, 043001 (2025).

[42] W. R. Jie, Dataset for "High-resolution photoelectron spectroscopy and photodetachment rotational simulations of SeH- and TeH-" [Data set], Zenodo (2025), https://doi.org/10.5281/zenodo.17873894.